

Traffic-induced multicomponent ultrafine particle microphysics in the WRF v3.6.1 large eddy simulation model

Zhong, Jian; Nikolova, Irina; Cai, Xiaoming; MacKenzie, A. Robert; Alam, Salim; Xu, Ruixin; Singh, Ajit; Harrison, Roy

DOI:

[10.1016/j.atmosenv.2019.117213](https://doi.org/10.1016/j.atmosenv.2019.117213)

License:

Creative Commons: Attribution-NonCommercial-NoDerivs (CC BY-NC-ND)

Document Version

Peer reviewed version

Citation for published version (Harvard):

Zhong, J, Nikolova, I, Cai, X, MacKenzie, AR, Alam, S, Xu, R, Singh, A & Harrison, R 2020, 'Traffic-induced multicomponent ultrafine particle microphysics in the WRF v3.6.1 large eddy simulation model: general behaviour from idealised scenarios at the neighbourhood-scale', *Atmospheric Environment*, vol. 223, 117213. <https://doi.org/10.1016/j.atmosenv.2019.117213>

[Link to publication on Research at Birmingham portal](#)

General rights

Unless a licence is specified above, all rights (including copyright and moral rights) in this document are retained by the authors and/or the copyright holders. The express permission of the copyright holder must be obtained for any use of this material other than for purposes permitted by law.

- Users may freely distribute the URL that is used to identify this publication.
- Users may download and/or print one copy of the publication from the University of Birmingham research portal for the purpose of private study or non-commercial research.
- User may use extracts from the document in line with the concept of 'fair dealing' under the Copyright, Designs and Patents Act 1988 (?)
- Users may not further distribute the material nor use it for the purposes of commercial gain.

Where a licence is displayed above, please note the terms and conditions of the licence govern your use of this document.

When citing, please reference the published version.

Take down policy

While the University of Birmingham exercises care and attention in making items available there are rare occasions when an item has been uploaded in error or has been deemed to be commercially or otherwise sensitive.

If you believe that this is the case for this document, please contact UBIRA@lists.bham.ac.uk providing details and we will remove access to the work immediately and investigate.

1
2

3 **Traffic-induced multicomponent ultrafine particle**
4 **microphysics in the WRF v3.6.1 large eddy simulation**
5 **model: General behaviour from idealised scenarios at**
6 **the neighbourhood-scale**
7

8
9 **Jian Zhong¹, Irina Nikolova¹, Xiaoming Cai^{1*},**
10 **A. Rob MacKenzie^{1,2}, Mohammed S. Alam¹, Ruixin Xu¹,**
11 **Ajit Singh¹ and Roy M. Harrison^{1,†}**
12

13 **¹School of Geography, Earth & Environmental Sciences**
14 **University of Birmingham**
15 **Edgbaston, Birmingham, B15 2TT**
16 **United Kingdom**
17

18 **²Birmingham Institute of Forest Research**
19 **University of Birmingham**
20 **Edgbaston, Birmingham, B15 2TT**
21 **United Kingdom**
22

23
24

* **Corresponding Author:** Xiaoming Cai (x.cai@bham.ac.uk)

† **Also at:** Department of Environmental Sciences / Center of Excellence in Environmental Studies, King Abdulaziz University, PO Box 80203, Jeddah, 21589, Saudi Arabia

25 **HIGHLIGHTS**

26
27
28
29
30
31
32
33
34

- 1) Multicomponent microphysics of UFPs is coupled with the WRF-LES model.
- 2) General behaviour of UFPs on the neighbourhood scale dispersion is investigated.
- 3) The combined effects of emissions, mixing and microphysics of UFPs are revealed.

35 **ABSTRACT**

36 Traffic is the key source of ultrafine particles (UFPs, particulate matter with an aerodynamic diameter
37 less than 0.1 μm or 100 nm) in most urban areas. The traffic-generated UFPs vented out from an
38 urban street mix with overlying ‘urban background air’ and are diluted whilst also undergoing change
39 due to condensation/evaporation and other aerosol microphysics. Traffic-generated UFPs are
40 comprised of a complex mixture of semi-volatile compounds (SVOCs) with volatility varying over
41 many orders of magnitude, resulting in size-dependent particle composition. This study coupled the
42 multicomponent microphysics (involving condensation/evaporation) of UFPs with the WRF v3.6.1
43 (Weather Research and Forecasting) large eddy simulation model (i.e. WRF-LES-UFP), and used
44 this modelling system to investigate the general behaviour of UFPs on the neighbourhood scale (10-
45 1,000 m; transport times of few minutes) for idealised scenarios. The model captures the horizontal
46 dispersion of UFPs downwind into the neighbourhood scale and vertical mixing with urban
47 background air. Evaporation decreases the mode size of UFPs venting into the urban boundary layer
48 from street-level. The neighbourhood-scale evolution of UFPs is, therefore, a combination of the
49 effects of emissions, mixing with background, and condensation/evaporation. Total UFP number
50 concentration and total mass concentrations scale linearly with the emission rate or the background
51 concentration, demonstrating numerical conservation of the scheme. The linearity is less pronounced
52 for the number concentration of smaller particles (UFP diameter less than 100 nm) with respect to
53 UFP size and concentrations of those carbon components with a time scale comparable to the dilution
54 time scale (in the order of minutes), reflecting the effects (altering the particle sizes) due to
55 condensation/evaporation.

56

57 **Keywords:** Atmospheric nanoparticles; Urban pollution; Aerosol microphysics; Urban Street; Semi-
58 volatiles.

59

60 1. INTRODUCTION

61 Ultrafine particles (UFPs or $PM_{0.1}$, particulate matter with an aerodynamic diameter $D_p < 0.1 \mu m$) are
62 respirable (Manigrasso et al., 2017) and may cause adverse health effects to the pulmonary system,
63 and the cardiovascular/nervous systems (e.g. Panis et al., 2010; Geiser et al., 2005). Unlike larger size
64 fractions PM_{10} ($D_p < 10 \mu m$) and $PM_{2.5}$ ($D_p < 2.5 \mu m$) (US EPA, 2017; European Commission, 2017),
65 there are currently no ambient air quality regulations for UFPs. UFPs dominate particle size number
66 concentrations (Harrison et al., 2000) and have received increasing attention from the scientific
67 community (e.g. Dall'Osto et al., 2011; Harrison et al., 2011; Vu et al., 2017; Jacobson et al., 2005).
68 UFPs from vehicle emissions, which tend to dominate the urban atmosphere (Harrison et al., 2018;
69 Kumar et al., 2014), contain multi-components of semi-volatile compounds (SVOCs) (Alam et al.,
70 2016; Baldauf et al., 2016), contributing to the changes in particle size due to
71 condensation/evaporation (Harrison et al., 2016; Jacobson et al., 2005).

72

73 Condensation and evaporation are among the most important aerosol microphysical processes in
74 predicting the fate of ultrafine particles in urban air (Gelbard and Seinfeld, 1980; Harrison et al.,
75 2016; Jacobson, 2005; Jacobson and Turco, 1995; Jacobson et al., 1996; Pankow, 1994). Nikolova et
76 al. (2016) developed a CiTTy-Street-UFP box model, an urban version of CiTTyCAT Lagrangian
77 model (Pugh et al., 2012) including aerosol microphysics. The model was used to assess the
78 importance of microphysical processes and to simulate the behaviour of traffic-related UFPs within
79 a street canyon and UFP evolution from canyon rooftop to a nearby downwind urban park. For a
80 steady-state simulation of number concentration in the canyon, there is a balance among the traffic-
81 related UFP emissions, aerosol microphysics, and exchange with the rooftop air. There is also
82 evidence of the evaporation of UFPs when the rooftop air is advected to the neighbourhood park.
83 Nikolova et al. (2018) further used this box model approach to investigate the influence of particle
84 composition on the evolution of particle size distributions at the time scale of 100s (related to the
85 dispersion at the neighbourhood scale). The evaporative shrinkage of UFPs from the nucleation mode

86 was highly influenced by SVOC composition. Zhong et al. (2018) coupled the UFP multicomponent
87 microphysics (i.e. evaporation/condensation of SVOCs) with a two-box model for urban street
88 canyon compartments and investigated factors that may inhibit mixing. The contrasts in the UFP
89 number-size distribution between the lower and upper canyons are captured by this two-box-UFP
90 canyon model. The traditional assumption of a one box model for a compartmentalised canyon would
91 typically under-predict the UFP number concentration in the lower canyon compared with the
92 proposed two-box model. The traffic-generated nanoparticles vented out from an urban street
93 network, which may be simulated by a street canyon box model (Nikolova et al., 2016), could be
94 evaporated to smaller particles while they are transported during neighbourhood scale dispersion
95 (Dall'Osto et al., 2011; Harrison et al., 2019).

96

97 According to the horizontal length scale, Britter and Hanna (2003) classified the atmospheric flow
98 and related phenomena (e.g. dispersion of pollutants) into four categories: i.e. regional scale (~100-
99 200 km), urban/city scale (~10-20 km), neighbourhood scale (~1-2 km) and local/street scale (~0.1-
100 0.2 km). The neighbourhood scale has been increasingly concentrated on by the urban research
101 community. This is a scale over which the computation can be feasible at high spatial and temporal
102 resolution (Carpentieri et al., 2012).

103

104 The large-eddy simulation (LES) mode of the Weather Research and Forecasting (WRF) model
105 (WRF-LES) (Skamarock and Klemp, 2008) is a powerful tool to simulate the turbulence-resolved
106 atmospheric flow at the neighbourhood scale in 3-dimensional (3D) Eulerian grids with high spatial
107 and temporal resolutions. Nottrott et al. (2014) investigated the dispersion of a passive scalar from
108 continuous point sources within the atmospheric boundary layer using the WRF-LES. The plume
109 trajectories were captured by the model. Nunalee et al. (2014) also simulated the plume impingement
110 of a passive scalar in the atmospheric turbulent flow influenced by complex terrain features. The
111 spatial pattern of the surface plume trajectory was well revealed by the WRF-LES. Jacobson and

112 Seinfeld (2004) investigated the dispersion and the evolution of soot particle size distributions from
113 both point and line sources using a 3D global-through-urban atmospheric model. There was a
114 reduction in the particle number concentrations downwind of the emission sources, primarily due to
115 dilution. The WRF-CHEM mesoscale model (Grell et al., 2005) provides the capability of coupling
116 WRF with “online” chemistry involving several aerosol schemes, such as GOCART (From the
117 Goddard Chemistry Aerosol Radiation and Transport model) (Chin et al., 2000), MOSAIC (Model
118 for Simulating Aerosol Interactions and Chemistry) (Zaveri et al., 2008) and MADE/SORGAM (The
119 Modal Aerosol Dynamics Model for Europe with secondary organic aerosols) (Ackermann et al.,
120 1998; Schell et al., 2001). However, there is no aerosol size information for GOCART, only 4 or 8
121 size bins up to PM_{10} for MOSAIC and 3 log-normal aerosol modes (i.e. Aitken, accumulation and
122 coarse) for MADE/SORGAM. There are currently no prior studies using WRF-LES at the
123 neighbourhood/micro scale and multicomponent aerosol microphysics for UFPs at the nanoparticle
124 scale.

125
126 In this study, the multicomponent microphysics (i.e. condensation/evaporation) of UFPs is coupled
127 with WRF-LES (WRF-LES-UFP) to simulate the evolution and dispersion of UFPs at the
128 neighbourhood scale for idealised scenarios of road emissions. The UFP code was previously
129 implemented into CiTTY-Street-UFP (Nikolova et al., 2016) and the compartmentalised canyon box
130 model (Zhong et al., 2018). Condensation and evaporation in the presence of semi-volatiles are
131 processes that can actively re-partition semi-volatiles between gas and particle, alter the sizes of the
132 UFPs and change the chemical composition of UFPs. With the proposed model (WRF-LES-UFP),
133 we can explore a very complex system of interactions between particles, emissions, atmosphere and
134 mixing, and quantify those interactions.

135

136

137

138 2. METHODS

139 2.1 The WRF-LES Model

140 The WRF-LES model explicitly calculates the larger resolved eddies with the smaller unresolved
141 eddies parameterised by subgrid-scale (SGS) turbulence models (Moeng et al., 2007) and can be used
142 for the neighbourhood scale simulation. LES simulations, therefore, allow for intermittency in
143 turbulence in a way that cannot be captured by Reynolds-average Navier-Stokes (RANS) (e.g.
144 Solazzo et al., 2008; Baik et al., 2007; Kwak and Baik, 2014) or semi-analytical Gaussian dispersion
145 methods (e.g. McHugh et al., 1997; Popoola et al., 2018; Munir and Habeebullah, 2018). The filtered
146 continuity and Navier-Stokes equations can be described as follows (Munoz-Esparza et al., 2015):

$$147 \frac{\partial \tilde{u}_i}{\partial x_i} = 0, \quad (1)$$

$$148 \frac{\partial \tilde{u}_i}{\partial t} + \frac{\partial \tilde{u}_i \tilde{u}_j}{\partial x_j} = \nu \frac{\partial^2 \tilde{u}_i}{\partial x_j \partial x_j} - \frac{1}{\tilde{\rho}} \frac{\partial \tilde{p}}{\partial x_i} - \frac{\partial \tau_{ij}}{\partial x_j} + f_c \epsilon_{ij3} (\tilde{u}_j - U_{g,j}), \quad (2)$$

149 where \tilde{u}_i represents the i^{th} component of resolved velocity with i (or j) = 1, 2, 3 indicating x, y, z
150 directions; x_i (or x_j) denotes the i^{th} (or j^{th}) component of spatial coordinates; t is time; \tilde{p} is the resolved
151 pressure; $\tilde{\rho}$ is the resolved density; f_c denotes the Coriolis parameter due to the rotation of Earth (here,
152 $f_c = 1.139 \times 10^{-4} \text{s}^{-1}$, representing a latitude of 51.526 N); ϵ_{ij3} denotes the alternating unit tensor;
153 $U_{g,j}$ denotes the geostrophic wind; ν is the kinematic molecular viscosity; τ_{ij} denotes the SGS stress
154 tensor, which is parameterised by the 1.5-order turbulent kinetic energy (TKE) SGS model (See
155 Section A in the Supplementary Material for details).

156 2.2 Size-Dependent Multicomponent Microphysics of UFPs

157 The multicomponent microphysics of UFPs considered in the current WRF-LES model include the
158 condensation and evaporation processes of SVOCs, which are the dominant microphysical processes
159 in predicting the neighbourhood scale evolution of UFPs in urban air (Nikolova et al., 2016). For the
160 purpose of this study, coagulation and deposition processes have been omitted as these play a far
161 lesser role than evaporation processes on the short timescales of neighbourhood atmospheric transport

162 (Nikolova et al., 2016). Nikolova et al. (2016) suggested that the exclusion of coagulation (with a
 163 coagulation kernel accounting for Brownian motion) and deposition processes in the street canyon
 164 model would lead to a reduction of the total particle number by 4.7% - 8.2% depending on the
 165 ventilation conditions. Jacobson et al. (2005) suggested that Brownian motion together with van der
 166 Waals/viscous forces and fractal geometry were the three most important processes in the treatment
 167 of coagulation kernel and it was essential to consider both evaporation and coagulation in the model
 168 for nanoparticles below 15 nm near a roadway, especially when there was a peak diameter less than
 169 10 nm for the nucleation mode. In this current modelling study, we focus on the relative importance
 170 of the processes, i.e. mixing vs. condensation and evaporation processes, emission vs. background.
 171 By using the sectional modelling approach, the mass transfer rate between particulate and gas phases
 172 due to the condensation and evaporation processes for the q -th component SVOC of one particle in
 173 the jb -th size bin can be estimated as follows (Jacobson, 2005):

$$174 \frac{d\tilde{m}_{q,jb}}{dt} = a_{FS}^{jb} \frac{2\pi D_p^{jb} M_q D_q}{RT} (e_q^\infty - X_{q,jb} a_K^{q,jb} e_q^{vap}), \quad (3)$$

175 where q is for the q -th component; jb is for jb -th size bin; a_{FS} is the Fuchs-Sutugin correction factor;
 176 D_p represents the particle diameter (m); M is the molar mass (g mol^{-1}); D_q denotes the vapour
 177 diffusivity ($\text{m}^2 \text{s}^{-1}$); R is the universal gas constant ($\text{J mol}^{-1} \text{K}^{-1}$); T is the temperature (K); e_q^∞ is the
 178 partial pressure in the ambient air (Pa); X is the molar fraction; a_K accounts for the Kelvin effect;
 179 e_q^{vap} is the saturation vapour pressure (Pa), i.e. the vapour pressure of the chemical species
 180 evaporating from the particle surfaces. e_q^∞ is derived from the gas-phase concentration of component
 181 q based on the ideal gas law, while e_q^{vap} is based on the method of (Compernelle et al., 2011) found
 182 in the UManSysProp online tool (Topping et al., 2016). The saturation vapour pressure using the
 183 method of Compernelle et al. (2011) was tested and compared with other vapour pressure estimation
 184 methods in Nikolova et al. (2018) and informed by measurements of vapour pressure made in our
 185 laboratory (Alam et al., 2019).

186 Table 1 shows the initial partial pressure at the inlet of the model and the saturation vapour pressure
 187 estimated at temperature of 284.15 K based on the UManSysProp online tool using data from
 188 Compernelle et al. (2011). When $\frac{d\tilde{m}_{q,jb}}{dt} > 0$ in Equation 3, vapour condenses on the particles; when
 189 $\frac{d\tilde{m}_{q,jb}}{dt} < 0$ in Equation 3, evaporation of SVOCs from the particle phase takes place. The overall
 190 production of gaseous component q due to multicomponent microphysics of UFPs can be calculated
 191 as:

$$192 \quad \Delta\tilde{c}_q = - \sum_{jb} \tilde{N}_{jb} \frac{d\tilde{m}_{q,jb}}{dt}, \quad (4)$$

193 where \tilde{N}_{jb} is the number concentration for the jb -th size bin. A dynamical size (d_{jn}) is calculated for
 194 each size bin after the condensation and evaporation processes and a redistribution scheme is
 195 implemented to redistribute both UFP number and mass concentrations to the sectional bin (See
 196 Section B in the Supplementary Material for details).

197 The UFP composition in our default UFP module configuration includes 18 components, i.e. 1 non-
 198 volatile core and 17 surrogate n-alkane components (SVOCs), i.e. C₁₆H₃₄-C₃₂H₆₆ (labelled ‘C16’ –
 199 ‘C32’, below). The hundreds of SVOC components found in UFP (Alam et al., 2016) are mapped
 200 onto these surrogates on the basis of their volatility (Nikolova et al., 2018) (See Table S1 in the
 201 Supplementary Material for the volatility bin information, grouped n-alkane/surrogate n-alkane used
 202 in this study). These volatility classes are derived based on the GC × GC chromatogram with the same
 203 carbon numbers in different carbon arrangements (e.g. straight-chain or branched-chain) (Alam et al.,
 204 2016). Particle size is sectioned into 15 equally-sized bins on a logarithmic scale, covering particles
 205 with geometric mean diameter of 6.7 nm – 501.4 nm. There are 17 SVOC components in the gas-
 206 phase, corresponding to each surrogate n-alkane. The UFP number concentration of each size bin is
 207 updated diagnostically based on the total mass concentration of the size bin.

208 **2.3 Framework of WRF-LES-UFP Coupling**

209 The dispersion of tracers (for both multicomponent particulate and gas phases) in the WRF-LES
210 model is described as follows. For the multicomponent particulate phase:

$$211 \frac{\partial \tilde{Q}_{q,jb}}{\partial t} + \frac{\partial}{\partial x_j} (\tilde{Q}_{q,jb} \tilde{u}_j) = \frac{\partial}{\partial x_j} \left(K_c \frac{\partial \tilde{Q}_{q,jb}}{\partial x_j} \right) + \Delta \tilde{Q}_{q,jb} + E_{q,jb}, \quad (5)$$

212 where \tilde{Q} represents the resolved UFP mass concentration; “ q ” denotes the q -th component; “ jb ”
213 denotes the jb -th size bin; K_c is the SGS eddy diffusivity; $\Delta \tilde{Q}$ and $E_{q,jb}$ represent the resolved source
214 terms due to multicomponent microphysics of UFPs (i.e. the condensation/evaporation processes
215 included in the current study) and emissions, respectively.

216

217 For the multicomponent gas phase,

$$218 \frac{\partial \tilde{c}_q}{\partial t} + \frac{\partial}{\partial x_j} (\tilde{c}_q \tilde{u}_j) = \frac{\partial}{\partial x_j} \left(K_c \frac{\partial \tilde{c}_q}{\partial x_j} \right) + \Delta \tilde{c}_q + E_q, \quad (6)$$

219 where \tilde{c}_q represents the resolved gas concentration for component q ; $\Delta \tilde{c}_q$ and E_q represent its resolved
220 source terms due to multicomponent microphysics of UFPs and emissions, respectively. The resolved
221 source terms for both particulate and gas phases in Equations 5-6 are derived from the UFP
222 multicomponent microphysics module (involving condensation/evaporation), as in previous canyon
223 box models (Nikolova et al., 2016; Zhong et al., 2018; Nikolova et al., 2018).

224

225 **2.4 WRF-LES-UFP Model Configuration and Scenarios**

226 To demonstrate the capabilities of the WRF-LES-UFP model, we choose an idealised urban scenario
227 driven by realistic environmental conditions and boundary conditions. Such an idealised scenario
228 allows us to diagnose more readily the UFP dynamics. The WRF-LES computational domain used in
229 this study (Figure S1 in the Supplementary Material) covered a horizontal area of $2.54 \text{ km} \times 2.54 \text{ km}$
230 ($L_x \times L_y$) with $20 \text{ m} \times 20 \text{ m}$ resolution. The vertical domain size is 1 km (L_z) with 79 stretch grids, so

231 the number of cells in the domain is $127 \times 127 \times 79$. Because the length scales of the underlying
232 building geometries and street canyons are about same as the grid resolution adopted here (20 m), it
233 is not appropriate to resolve these structures explicitly. It is assumed that the height and roughness of
234 the canopy vary slowly relative to the grid resolution, and a homogeneous urban canopy is used in
235 this study. To focus on the evolution of multicomponent UFPs at the neighbourhood scale above the
236 urban canopy (instead of building scale inside the urban canopy), we adopt a simplified approach of
237 setting up the first vertical cell at a nominal ‘rooftop level’ and specifying momentum flux and heat
238 flux at the bottom of the domain using observational data as discussed below.

239

240 A fixed time step of 0.2 s is adopted for the airflow calculation, whilst an adaptive time step is used
241 for solving multicomponent condensation/evaporation of UFPs. Periodic lateral boundary conditions
242 are specified for velocity components. Inlet conditions for the SVOC quantities (gas concentrations,
243 particle number concentration size distributions, and particle SVOC mass fractions) are specified as
244 fixed values. At the outlet, a zero-gradient condition is specified for all SVOC quantities.

245

246 Weather conditions adopted for the simulations are informed by observational data (Heathrow
247 airport) for the $180^\circ \pm 25^\circ$ wind sector during the London campaign (Jan-Feb 2017) (see Harrison et
248 al. (2019) for details). The geostrophic wind is specified as $U_g=5 \text{ m s}^{-1}$ and $V_g=10 \text{ m s}^{-1}$ and in the
249 presence of the Coriolis force, this attempts to achieve an approximate southerly wind of 2 m s^{-1} near
250 the rooftop ‘surface’ at the bottom of the model domain. An upwelling surface sensible heat flux of
251 13 W m^{-2} (tke_heat_flux in the WRF namelist.input option) is adopted for the lower boundary
252 condition of heat and a surface drag coefficient of 0.048 (tke_drag_coefficient in the namelist.input
253 option) is specified for the lower boundary condition of momentum, derived from eddy-covariance
254 measurements at the rooftop of Regent's University during the campaign.

255

256 The boundary layer height is initially ~ 500 m, specified by an initial constant vertical potential
257 temperature of 282.15 K for the lower 475 m, capped by a strong inversion with of $\partial T/\partial z = 0.05$ K
258 m^{-1} from 475 m to 625 m and $\partial T/\partial z = 0.003$ K m^{-1} from 625 m to the domain top. The meteorological
259 conditions of a low sensible heat flux at the ground and a strong capping inversion lead to a nearly
260 constant height of the boundary layer during the simulation period. A damping layer of 300 m is
261 applied near the domain top to prevent gravity waves. WRF-LES was run without the UFP module
262 for 8 hours as a spin-up period in order to achieve a quasi-steady flow. Then the UFP module was
263 switched on for 30 min, sufficiently long compared with the timescale of the geostrophic wind
264 advection across the domain which is about 4 min. The output of the last 10 min with an interval of
265 3 s was used for analysis.

266

267 An idealised street (represented by a line emission perpendicular to the surface wind direction) with
268 a width of 40m is configured in the middle of the domain (Figure S1 in the Supplementary Material).
269 The emission fluxes to the first vertical model level is based on those from vehicles directly into the
270 street canyon. In this study, we introduce a BASE case scenario and the settings are as follows. The
271 emission factor for total UFP number is 7.93×10^{13} particles vehicle $^{-1}$ km $^{-1}$, which is based on the
272 value from Jones and Harrison (2006) with a correction factor for the year of 2017 derived from an
273 analysis of measurement data (Harrison et al., 2019). The traffic activity is specified as 3740 vehicle
274 hour $^{-1}$ at a heavily trafficked street (Marylebone Road) for the 180° wind sector during the campaign
275 in London (Harrison et al., 2019).

276

277 The size distribution of emitted UFPs is comprised of three log-normal distributions with peaks at 21
278 nm, 29 nm and 69 nm, respectively, which are derived from the mode fitting for particle size
279 distributions of the traffic increment, i.e. the background subtracted from Marylebone Road
280 measurement at the 180° wind sector (Harrison et al., 2019). The mass fraction of non-volatile core

281 is assumed to be 1 % for the nucleation mode (Nikolova et al., 2016), gradually increasing to 90 %
282 for the Aitken mode and 99 % for the accumulation mode. The mass fraction of SVOC compounds
283 in the emitted UFPs is then scaled by the measured UFP composition in samples collected in
284 Marylebone Road (Harrison et al., 2018).

285

286 The emission factors of total grouped SVOCs (from C16 to C32) are $681 \mu\text{g veh}^{-1} \text{km}^{-1}$ for the gas
287 phase and $1714 \mu\text{g veh}^{-1} \text{km}^{-1}$ for the particle phase (See details in Table S2 in the Supplementary
288 Material). The UFP size distribution at the inlet of the domain is based on the mode fitting of BT
289 tower measurements (160 m above ground level) for the 180° wind sector during the campaign in
290 London (Harrison et al., 2019), which has 3 log-normal distributions with peaks at 24 nm, 66 nm and
291 163 nm, respectively. The SVOC concentrations (gas and particles) at the inlet of the domain are
292 based on the scaled Regent's Park measurements (inferred from the ratio of black carbon measured
293 at BT tower to that measured at Regent's Park) (See Table S3 in the Supplementary Material for inlet
294 SVOC concentrations). The inlet air parcel may be slightly adjusted by the multicomponent
295 microphysics of UFPs to reach a quasi-equilibrium state after a certain travelling distance and we
296 take 200 m before the emission at the bottom level of the domain (Figure S1 in the Supplementary
297 Material) as the inflowing background in the analysis of the model output.

298

299 In order to investigate the effect of emissions, cases with changes in emissions only for both gas and
300 particle phases are configured (i.e., multiplying by a coefficient, $\beta=[0.5, 0.75, 1.25, 1.5]$, the
301 emissions in the BASE case) and named EM0.5, EM0.75, EM1.25, and EM1.5, respectively. In order
302 to investigate the effect of inlet background, cases with changes in inlet background only for both gas
303 and particulate phases are configured using a coefficient $\alpha=[0.5, 0.75, 1.25, 1.5]$, i.e. case BG0.5,
304 BG0.75, BG1.25, and BG1.5. We perform a linearity analysis by investigating the sensitivity to
305 emissions and inlet background concentrations in both gas and particle phases.

306

307 **3. RESULTS AND DISCUSSION**

308 **3.1 The BASE Case Output from the model**

309 **3.1.1 Total UFP number concentration**

310 Figure 1(a) illustrates a vertical slice of the total UFP number concentration (UFPNC), which is
311 averaged horizontally in the cross-wind direction and temporally over the final 10 min simulation;
312 this gives an indication of cross-sectional dispersion of UFPs for the BASE case in the model. The
313 total UFPNC is gradually diluted by a southerly wind from the street (the west-east line emission) to
314 its northerly neighbourhood. The vertical expansion of the plume is observed as UFPs are advected
315 downwind into the neighbourhood scale and vertically mixed with urban background air.

316

317 Similar neighbourhood dispersion behaviour was also observed by other simulations, i.e. Nottrott et
318 al. (2014) and Nunalee et al. (2014) for the dispersion of a passive scalar from point sources and
319 Jacobson and Seinfeld (2004) for the dispersion of soot particles from both point and line sources.
320 The spatial pattern also indicates the neighbourhood dispersion of UFPs with a decrease of the total
321 UFP number concentration downwind of the emission. This is consistent with classical line-source
322 dispersion (Munir and Habeebullah, 2018; Jacobson and Seinfeld, 2004) and with the measured data
323 which demonstrate that the UFPNCs in Marylebone Road were always much higher than those at its
324 downwind neighbourhood rooftop site in Regent's Park (Dall'Osto et al., 2011; Harrison et al., 2019).

325

326 Figure 1(b) shows a vertical slice of the ratio of concentration fluctuation intensity to mean
327 concentration for total UFPNC for the BASE case in the model. The concentration fluctuation
328 intensity is defined as $C' = \sqrt{(C - C_m)^2}$, where C_m represents a spatial and temporal average defined
329 earlier. The value of C'/C_m can be interpreted as the percentage of particle number fluctuation
330 intensity in relation to its mean value caused by the unsteady turbulence generated within the LES
331 simulation. The region upwind of emission is more determined by the fixed inlet conditions and

332 therefore has no significant concentration fluctuation. Once emissions are released, there is a plume
333 expansion for the concentration fluctuation intensity in the downwind side of the emission line.

334

335 Figure 1(c) illustrates the total UFPNC (both mean concentrations and concentration fluctuation
336 intensities) along a South-North line at the bottom model level (corresponding to just above rooftop
337 height) as a further indication of neighbourhood dilution. The highest value indicates the effect of
338 emissions from the street, which is similar to Figure 7(a) in Jacobson and Seinfeld (2004) for the
339 point source dispersion. The total UFPNC decreases rapidly at the near-source downwind
340 neighbourhood, gradually approaching the background levels. This is due to the expansion of plume
341 as it traverses its neighbourhood downwind (Figure 1(a)). In general, the total UFPNC appears to
342 behave like a passive scalar, as expected from the model's number-conserving numerics and lack of
343 (because assumed slow (Nikolova et al., 2016; 2018)) coagulation, deposition, and gas-phase
344 chemistry.

345

346 **3.1.2 UFP number-size distribution**

347 Figure 2(a) illustrates the spatially (west-east) and temporally (the final 10 min period) averaged UFP
348 number-size distribution (UFPNSD), together with its fluctuation intensity (indicated by shaded
349 areas), for several downwind locations at the bottom level of the domain (corresponds to the urban
350 canopy above rooftop height) for the BASE case in the model. The black line in Figure 2(a) represents
351 the inflowing background (200 m before the emission at the bottom level of the domain). The red line
352 with circles at the top of the graph is for the UFPNSD of the south-side rooftop cell of the line
353 emission source. For comparison of mode sizes, the red line with triangles at the bottom is for UFP
354 emission rate; other lines are for the UFPNSD at downwind distances of 100 m and 400 m (or
355 travelling time of about 50 s and 200 s), respectively. Within each WRF-LES time step of 0.2 s, both
356 south-side and north-side rooftop cells at the line emission source receive a given amount of emitted
357 pollutants (both particle and gas phases) and the execution of WRF's advection and diffusion modules

358 brings some fresher air advected from the upwind neighbour cells. Then the UFP module is applied
359 to the mixed air parcel and to yield a new UFPNSD for the south-side rooftop cell, for example, as
360 shown by the top curve in Figure 2(a). Comparison of this curve with the emission curve gives a clear
361 indication of the direct influence of emission, e.g. by their same peak diameter values (peaked at bin
362 5 with bin bounds of [19.8 nm, 26.9 nm]). The small fluctuations of UFPNSD for the Aitken and
363 accumulation modes (i.e. large size bins in Figure 2(a)) is explained by large fractions (90%-99%) of
364 non-volatile core for this mode. An increase in the non-volatile core fraction will result in a decrease
365 in the evaporative SVOCs (Nikolova et al., 2018).

366

367 There is a reduction in UFPNSD and fluctuations along the downwind distance in the simulation.
368 There is also a clear shift of the peak particle size from the rooftop (peaked at bin 5 with bin bounds
369 of [19.8 nm, 26.9 nm]) to its downwind locations of both 100m and 400 m (peaked at bin 4 with bin
370 bounds of [14.6 nm, 19.8 nm]). This shift indicates particle evaporation during the neighbourhood
371 dispersion of UFPs. The UFPNSD within the downwind neighbourhood is, therefore, a result of a
372 combination of mixing and aerosol microphysics (i.e., condensation/evaporation of SVOCs). In the
373 measurement in Harrison et al. (2019), there is also clear evidence of the shrinkage of particle sizes
374 from the roadside (MR_OBS in Figure 2a with a peak diameter falling into bin 5 [19.8 nm, 26.9 nm]
375 as defined in the model) to nearby downwind rooftop location (RU_OBS in Figure 2a with a peak
376 diameter falling into bin 4 [14.6 nm, 19.8 nm] as defined in the model), with the lower diameter limits
377 of 10 nm and 16 nm by the instruments adopted. This suggests that the current model can capture the
378 general behaviour of particle size shrinkage mainly due to evaporation. The exclusion of coagulation
379 process in our model may lead to an overestimation in the number concentration for particles below
380 15 nm, as suggested by Jacobson et al. (2005) with a peak diameter less than 10 nm for the nucleation
381 mode. Since the nucleation mode in our model has a peak diameter higher than 15 nm, the effect of
382 coagulation process may be reduced. As there are many complex conditions in the real world
383 measurement that our current model is not able to fully represent, such as well-defined background

384 conditions, emission pattern, real meteorological conditions together with realistic landscape,
385 complex aerosol microphysics processes and other model input assumptions, it is difficult for us to
386 well match the exact number size distribution profile measured in the field campaign.

387

388 Figure 2(b) illustrates the dilution ratio, defined as $(C_{downwind} - C_{bg}) / (C_{rooftop} - C_{bg})$, of UFP size
389 fractions for downwind locations (rooftop+100m and rooftop+400m) for the BASE case in the model.
390 For UFP size fractions with diameter greater than 100 nm, the dilution ratio closely follows that of a
391 passive scalar (shown as size-independent dotted lines in Figure 2(b)). For these larger UFPs, the
392 neighbourhood dispersion is dominated by dilution, attributable to the large fraction of non-volatile
393 core in these particles. There are variations in dilution ratio for UFPs smaller than 100 nm, indicating
394 that both dilution and condensation/evaporation are competing during the neighbourhood dispersion.
395 Specifically, the number of medium-size particles ($20 \text{ nm} < D_p < 100 \text{ nm}$) is reduced more quickly
396 than the rate for a passive scalar, whereas the number of small-size particles ($D_p < 20 \text{ nm}$) is reduced
397 more slowly than the rate for a passive scalar. Because of the simplicity of our idealised scenario, we
398 can attribute this size-dependent behaviour to evaporation, which converts some medium-size
399 particles to smaller-sized ones during the advection-dilution process.

400

401

402 **3.1.3 SVOCs mass concentrations**

403 Figure 3(a-c) shows SVOC mass concentrations in both gas and particle phases at the rooftop and
404 downwind neighbourhood locations for the BASE case in the model. For low-carbon components
405 (C16-C18) having higher saturation vapour pressures (Table 1), the emissions are dominated by the
406 gas phase (Table S2) and their respective rooftop gas concentration increments (from the background)
407 are due to the vapour emissions. For the carbon components of C19-C22, the mass emissions are
408 dominated by the particle phase (Table S2). However, their rooftop particle concentration increments

409 (Figure 3b) are not significant, particularly for C19-C21. On the other hand, their rooftop gas
410 concentration increments are of large values (Figure 3a). This simulation clearly indicates that the
411 evaporation process proceeds very rapidly to generate higher gas concentrations (Figure 3a) before
412 the dispersion process takes effect. This can also be seen from the particle mass concentrations which
413 are very close to background levels at the rooftop although they are subject to particle emission fluxes
414 (Figure 3(b)). For C22, its rooftop particle concentration increment is about 8 ng m^{-3} (Figure 3(b)),
415 whereas its gas concentration increment is about 20 ng m^{-3} (Figure 3a).

416

417 For carbon components of C23 onwards, the mass emissions are still dominated by the particle phase
418 (Table S2), but their rooftop concentration increments are gradually shifted from gas phase to particle
419 phase. The contribution of evaporation is important during the neighbourhood dispersion process for
420 SVOCs having evaporation timescales of SVOCs (Table S4 in the Supplementary Material)
421 comparable to the dilution time scale (i.e. for C21-C26) (Nikolova et al., 2018). This is indicated by
422 the gas concentrations, especially for C24-C26, not decreasing appreciably during the neighbourhood
423 dispersion.

424

425 For higher carbon components (from C27 onwards), condensation/evaporation is relatively slow due
426 to their lower saturation vapour pressures (Table 1). The concentrations of these SVOCs in both gas
427 and particle phases are more dependent on the strength of both emissions and background. As the gas
428 emission fluxes are relatively smaller than particle, their gas-phase concentrations increase slightly
429 at the rooftop and then approach background levels after a downwind distance of 100m. The
430 increment due to emission is more significant in particle concentrations of these higher carbon
431 number SVOCs. During the dispersion process, condensation processes may occur due to the very
432 low saturation vapour pressures for some higher carbon components, e.g. C31-C32 (Table 1).

433

434 As shown in Figure 3(c), the rooftop generally has the highest concentrations (both mean and
435 fluctuation concentrations) for all SVOCs (the sum of gas and particle phase concentrations)
436 compared with the downwind locations. The SVOC concentrations rapidly decrease at a short
437 travelling distance and then approach the background levels during their neighbourhood-scale
438 dispersion. Because of mass conservation, each $C_{n, \text{gas+particle}}$ should behave like a passive scalar,
439 possessing the spatial patterns similar to total UFP number concentration shown in Figure 1, with
440 their own background concentration and peak concentration level near the line source. Figure 3(d)
441 illustrates the dilution ratio of SVOC gas and particle phases (defined in the same way as that for UFP
442 number concentrations in Figure 2(b)) for the downwind locations (rooftop+100m and
443 rooftop+400m). For both lower carbon gas-phase components (C16-C20) and higher carbon particle-
444 phase components (C27-C32), the dilution ratio closely follows that of a passive scalar (as indicated
445 by dashed lines, which are also the same as that in Figure 2(b)), indicating that dilution dominates
446 during their neighbourhood dispersion.

447

448 For C21-C26, there are variations of dilution ratios along the dashed lines (for a passive scalar)
449 indicating that aerosol condensation/evaporation plays an important role during the neighbourhood
450 scale dispersion. Their gas-phase mass concentrations are reduced more slowly than the rate for a
451 passive scalar (the dilution ratios are above the dashed lines) and their particle-phase mass
452 concentrations are reduced faster than the rate for a passive scalar (the dilution ratios are below the
453 dashed lines).

454

455 In summary, the above discussions suggest that the evaporation of low-carbon components (C16-
456 C20) of emitted particles is almost complete on the timescale of less than a second (Table S4 in the
457 Supplementary Material), and this leads to very high C_{gas} and negligible $C_{particle}$ at the rooftop (Figs
458 3(a) and 3(b)). From the rooftop location to the downwind locations of 100m and 400 m (or travelling

459 time of about 50 s and 200 s), C_{gas} for C16-C20 follows the dilution rate of a passive scalar (Figure
 460 3(d)). However, the evaporation of the medium-carbon components (C21-C26) of emitted particles
 461 is slower, taking the timescale of travelling from the rooftop to 100-400 m downwind (about 50 s and
 462 200 s). This evaporation process converts some medium-carbon component SVOCs from the particle
 463 phase to gas phase while the advection-dilution processes are underway during the period (Figure
 464 3(d)). Finally the evaporation (or condensation) of high-carbon components (C27-C32) of emitted
 465 particles is extremely slow and within the timescale of travelling, $C_{particle}$ behaves like the dilution
 466 of a passive scalar (Figure 3(d)).

467

468 **3.2 Linearity Analysis Among Cases from the model**

469 To provide insight into the relationships among multiple processes, the linearity of the dependence
 470 of several UFP quantities (UFPNSD, all-size particle mass concentration, gas mass concentration,
 471 and total mass concentration) on the emission rate and on the inlet background concentration, has
 472 been investigated. For this purpose, a scaled concentration for the ic^{th} case is defined as follows:

$$473 \hat{C}^{ic} = (C^{ic} - \alpha C_{bg}^{BASE}) / \beta, \quad (7)$$

474 where C^{ic} is the concentration of any quantity in the ic^{th} case, C_{bg}^{BASE} is the background concentration
 475 in Case BASE, α and β are the multiplied coefficients for inlet background and emission, respectively
 476 (defined in Sect. 2.3). If the linearity is perfect, the profile for any tested case (with the background
 477 subtracted) will scale exactly with total emission flux; in other words, the curves of scaled
 478 concentrations (\hat{C}^{ic}) for all tested cases should collapse into a single curve. Variations in the curves
 479 of scaled concentrations, \hat{C}^{ic} , would indicate nonlinear behaviour of the UFP system. This test
 480 determines whether a reduced microphysical model can be adopted or not: for perfectly scaled
 481 behaviour, results for one case can be used to construct the solutions for any multiplication of the
 482 emission profile and/or the background concentration profile.

483

484 Figure 4 demonstrates the perfect scalability for the spatially and temporally averaged total UFPNC
485 along a South-North line at the bottom level of the domain in the model. All the tested cases, with
486 varying either α or β , collapse onto a single curve, indicating an excellent scalability for total UFPNC.
487 This implies that if the results of a base case are known, the results for any other cases (corresponding
488 to a pair of α and β) can be obtained simply from the scaled equation (Equation 7), i.e. $\hat{C}^{ic} =$
489 $\beta \hat{C}^{BASE} + \alpha C_{bg}^{BASE}$.

490

491 For the rooftop location, there is weak non-linearity (not shown here) as the UFPNSDs are
492 predominately affected by emissions on a very short time scale (only influenced by lower carbon
493 components). Stronger non-linearity, for the downwind location of rooftop+400 m (travelling time of
494 about 200 s), is presented in Figure 5(a). The number concentrations for particles with diameters
495 higher than 100 nm exhibit a very good scalability. This is due to the large mass fraction of non-
496 volatile core in this size range, reducing the effects of evaporation/condensation, so that the behaviour
497 for these particles is very similar to that of passive scalars. For smaller particles, number
498 concentrations are not perfectly scaled. This is due to the nonlinear evaporation process for smaller
499 particles and the change of their particle sizes. If the scaled model (Equation 7) is used to generate an
500 approximate solution, then there would be an error for a non-perfectly scaled quantity (e.g. number
501 concentrations for smaller size bins). For the value range of α and β tested here, the errors are not
502 remarkably large, as illustrated in Fig 5. In order to reveal the details of the scalability, a correction
503 factor defining the error for the ic^{th} case (ϕ^{ic}) relative to case BASE for the scaled quantity is,

$$504 \phi^{ic} = (\hat{C}^{ic} - \hat{C}^{BASE}) / \hat{C}^{BASE}, \quad (8)$$

505

506 Figure 5(b) shows correction factors for selected nonlinear bins at the downwind location of
507 rooftop+400m in cases with varying background and emissions from the model. Correction factors

508 for selected bins are within 10% in most cases for varying emissions and varying background.
509 Correction factors for bin 3 (with bin bounds of [10.7 nm, 14.6 nm]) are generally bigger than those
510 for bin 7 ([36.6 nm, 49.9 nm]), followed by bin 5 ([19.8 nm, 26.9 nm]). For cases of varying
511 background, bin 3 always has an opposite sign compared to bins 5 and 7. From the discussion
512 associated with Figure 2(b) (the output of the BASE case), it is evident that the number concentration
513 of bin 3 increases with the evaporation from particles of bins 5-9. Furthermore, the discussions
514 associated with Figure 3(d) reveal that the evaporation occurs mainly to C21-C26 for a distance of
515 100-400m (travelling time of about 50 s and 200 s),. The decreasing trend of ϕ for “BG-bin3” with
516 α (indicator of the background concentrations’ magnitude) in Figure 5(b) suggests that higher
517 background SVOC concentrations will suppress the evaporation processes of C21-C26 in bins 5-9,
518 thus reducing particle numbers gained in bin 3. This finding is further supported by the increasing
519 trend of ϕ for “BG-bin7” with α in Figure 5(b), as suppressed evaporation causes fewer particle
520 numbers in bin 7 lost to smaller bins. It is interesting to see the trend of curve for “BG-bin5” is similar
521 to that for “BG-bin7”, suggesting the particles of bin 5 also contribute to evaporation which is
522 suppressed by higher background concentrations. This suppression of evaporation, however, is not
523 clearly seen for the “EM” cases in Figure 5(b).

524

525 Figure 6 shows the scaled concentrations for both SVOC gas and particle concentrations at the
526 downwind location of rooftop+400m (travelling time of about 200 s) from the model. There are very
527 good scalabilities for lower carbon components (e.g. C16-C22). This may be attributed to their high
528 vapour pressure and fast evaporation processes which would transfer particle SVOC mass to vapour
529 very quickly (Nikolova et al., 2018). Then this would be an effective dilution process for gas
530 concentrations (indicating nearly zero particle concentrations for lower carbon numbers in Figure
531 6(b)).

532

533 From C23-C27, the nonlinearity effect becomes more significant because SVOC vapour pressures
534 decrease with carbon number making evaporation slower. For those SVOCs having a timescale of
535 condensation/evaporation comparable to the dilution timescale, the effects of both
536 condensation/evaporation and neighbourhood dilution are significant, leading to significant
537 nonlinearity.

538

539 For higher carbon components (C28-C32), vapour pressures are very small (Table 1) and emission
540 rates are relatively smaller than lower carbon components, so only rather slow
541 condensation/evaporation processes occur. Their nonlinearities are less significant, with the dilution
542 process dominating, and only a slight influence of condensation/evaporation.

543

544 The sum of gas and particles (Figure 6(c)) can be scaled well although either gas or particles for
545 higher carbon components cannot be scaled well, indicating the evolving partitioning between gas
546 and particles. Figure 6(d) shows correction factors for a selected nonlinear carbon SVOC (C25) at
547 the downwind location of rooftop+400m in cases with varying background and emissions. These
548 correction factors can be up to around 60% for higher background cases and lower emission cases. A
549 consistent pattern is that, as α (or β) increases, the gas concentration of C25 decreases; in other words,
550 increasing α (or β) will suppress the evaporation of SVOCs on the particles. Correction factors for
551 gas concentrations always have opposite signs, and occur in a certain ratio to those for particle
552 concentrations, indicating that the conversion between gas and particles is conservative (Figure 6(c)).

553 This suggests a relationship of correction factors between gas and particles, i.e. $\phi_{gas}^{ic} / \phi_{particle}^{ic} =$
554 $-\hat{C}_{particle}^{BASE} / \hat{C}_{gas}^{BASE}$, which can also be inferred from Equations 7-8 assuming the conservation of the
555 sum of gas and particle concentrations ($\hat{C}_{gas}^{ic} + \hat{C}_{particle}^{ic} = \hat{C}_{gas}^{BASE} + \hat{C}_{particle}^{BASE}$). The asymmetric
556 patterns of correction factors between the gas phase and the particle phase in Figure 6(d) are due to
557 the BASE value for gas being lower than that for particles.

558

559 **4. CONCLUSIONS**

560 Size-dependent multicomponent microphysics of UFPs (involving condensation/evaporation of
561 SVOCs) has been coupled with WRF-LES to simulate the neighbourhood dispersion of UFPs for an
562 idealised line (street) emission. UFPs are horizontally advected downwind into the neighbourhood
563 scale and vertically mixed with urban background air. There is evidence of evaporation effects, which
564 alter the size distribution of UFPs. The lightest SVOCs evaporate within a model time step of 0.2 s,
565 while those in a middle range of carbon numbers (C21-C26) evaporate with a timescale about equal
566 to that of mixing. The dispersion and evolution of UFPs at the neighbourhood-scale are the result of
567 combined effects among emissions, mixing with background and evaporation/condensation.

568 Among a wide range of timescales for the evaporation/condensation of SVOCs (Table S4 in the
569 Supplementary Material), only those of the same order of magnitude as the travelling time have
570 significant contributions to the non-linear part of the UFP concentration field during the
571 neighbourhood-scale dispersion. There is a very good linearity for total UFPNC, UFPNSD (for UFP
572 diameter greater than 100 nm), concentrations of lower carbon components, and concentrations of
573 the sum of both gas and particles. The linearity is less precisely upheld for the number concentration
574 of smaller particles and concentrations of those carbon components with a timescale comparable to
575 the dilution timescale. For the non-perfectly scaled quantities, a linear model may be adopted to yield
576 an approximate solution with a tolerance of an error. For the value range of α and β tested in this
577 study, the errors are about 10% or less for the nucleation mode of particle number concentrations, but
578 can be as large as around 60% for the mass concentrations of medium-carbon SVOC components.

579

580 The WRF-LES-UFP model developed in this study reveals the evolution and dispersion of sized-
581 resolved UFPs from an urban street to its neighbourhood-scale surroundings and can be extended
582 straightforwardly to simulate the neighbourhood scale dispersion of UFPs for a realistic street canyon
583 network. Gridded surface emissions based on the real-time traffic reactivity can be implemented as

584 an input in the model to represent a real-world street network. Planned future modelling work is to
585 configure the model with a realistic street canyon network emission pattern and to conduct sensitivity
586 tests of key parameters under different atmospheric conditions.

587

588 **ACKNOWLEDGEMENTS**

589 This work is part of the FASTER project, ERC-2012-AdG, Proposal No. 320821 sponsored by the
590 European Research Council (ERC). JZ, XC, and ARMK gratefully acknowledge additional support
591 from the UK Natural Environment Research Council (NERC: NE/N003195/1 (JZ, XC, ARMK) and
592 NE/S013814/1 (XC, ARMK). The authors appreciate the regional HPC Midlands+ service
593 (<http://www.hpc-midlands-plus.ac.uk/>) and the University of Birmingham's BlueBEAR HPC service
594 (<http://www.bear.bham.ac.uk>) for providing the computational resources.

595

596 **CODE AVAILABILITY**

597 WRF v3.6.1 is available at http://www2.mmm.ucar.edu/wrf/users/download/get_sources.html. The
598 coupling WRF v3.6.1 large eddy simulation code with UFP microphysics module and case settings
599 are archived on Zenodo (<https://doi.org/10.5281/zenodo.3333811>).

600 **DATA AVAILABILITY**

601 Data supporting this publication are openly available from the UBIRA eData repository at
602 <https://doi.org/10.25500/edata.bham.00000366>

603

604

605 **REFERENCES**

- 606 Ackermann, I.J., Hass, H., Memmesheimer, M., Ebel, A., Binkowski, F.S., Shankar, U., 1998. Modal
607 aerosol dynamics model for Europe: Development and first applications. *Atmos. Environ.*, 32, 2981-
608 2999, 10.1016/s1352-2310(98)00006-5.
- 609
- 610 Alam, M.S., Zeraati-Rezaei, S., Stark, C.P., Liang, Z.R., Xu, H.M., and Harrison, R.M., 2016. The
611 characterisation of diesel exhaust particles - composition, size distribution and partitioning. *Faraday*
612 *Discuss.*, 189, 69-84, 10.1039/c5fd00185d,.
- 613
- 614 Alam, M.S., Nikolova, I., Singh, A., MacKenzie, A.R., Harrison, R.M., 2019. Experimental vapour
615 pressures of eight n-alkanes (C₁₇, C₁₈, C₂₀, C₂₂, C₂₄, C₂₆, C₂₈ and C₃₁) at ambient temperatures. *Atmos.*
616 *Environ.*, 213, 739-745.
- 617
- 618 Archer-Nicholls, S., Lowe, D., Darbyshire, E., Morgan, W.T., Bela, M.M., Pereira, G., Trembath, J.,
619 Kaiser, J.W., Longo, K.M., Freitas, S.R., Coe, H., McFiggans, G., 2015. Characterising Brazilian
620 biomass burning emissions using WRF-Chem with MOSAIC sectional aerosol. *Geosci. Model Dev.*,
621 8, 549-577, 10.5194/gmd-8-549-2015.
- 622
- 623 Baik, J.-J., Kang, Y.-S., Kim, J.-J., 2007. Modeling reactive pollutant dispersion in an urban street
624 canyon. *Atmos. Environ.*, 41, 934-949, 10.1016/j.atmosenv.2006.09.018.
- 625
- 626 Baldauf, R.W., Devlin, R.B., Gehr, P., Giannelli, R., Hassett-Sipple, B., Jung, H., Martini, G.,
627 McDonald, J., Sacks, J.D., Walker, K., 2016. Ultrafine Particle Metrics and Research Considerations:
628 Review of the 2015 UFP Workshop. *Int. J. Environ. Res. Public Health*, 13, 10.3390/ijerph13111054.
- 629
- 630 Britter, R. E., Hanna, S. R., 2003. Flow and dispersion in urban areas. *Annu. Rev. Fluid Mech.*, 35,
631 469-496, 10.1146/annurev.fluid.35.101101.161147.
- 632
- 633 Carpentieri, M., Salizzoni, P., Robins, A., Soulhac, L., 2012. Evaluation of a neighbourhood scale,
634 street network dispersion model through comparison with wind tunnel data. *Environ. Modell. Softw.*,
635 37, 110-124, 10.1016/j.envsoft.2012.03.009.
- 636
- 637 Chin, M., Rood, R.B., Lin, S.-J., Müller, J.-F., and Thompson, A.M., 2000. Atmospheric sulfur cycle
638 simulated in the global model GOCART: Model description and global properties. *J. Geophys. Res.:*
639 *Atmospheres*, 105, 24671-24687, 10.1029/2000jd900384.
- 640
- 641 Compernelle, S., Ceulemans, K., Muller, J.F., 2011. Evaporation: a new vapour pressure estimation
642 method for organic molecules including non-additivity and intramolecular interactions. *Atmos.*
643 *Chem. Phys.*, 11, 9431-9450, 10.5194/acp-11-9431-2011.
- 644
- 645 Dall'Osto, M., Thorpe, A., Beddows, D.C.S., Harrison, R.M., Barlow, J.F., Dunbar, T., Williams, P.
646 I., Coe, H., 2011. Remarkable dynamics of nanoparticles in the urban atmosphere. *Atmos. Chem.*
647 *Phys.*, 11, 6623-6637, 10.5194/acp-11-6623-2011.
- 648
- 649 European Commission: Air Quality Standards. 2017.
650 <http://ec.europa.eu/environment/air/quality/standards.htm>, 10.1016/s1352-2310(01)00438-1.
- 651
- 652
- 653

654 Geiser, M., Rothen-Rutishauser, B., Kapp, N., Schurch, S., Kreyling, W., Schulz, H., Semmler, M.,
655 Hof, V.I., Heyder, J., Gehr, P., 2005. Ultrafine particles cross cellular membranes by nonphagocytic
656 mechanisms in lungs and in cultured cells. *Environ. Health Perspect.*, 113, 1555-1560,
657 10.1289/ehp.8006.

658
659 Gelbard, F. & Seinfeld, J. H. 1980. Simulation of multicomponent aerosol dynamics. *Journal of*
660 *Colloid and Interface Science*, 78, 485-501, 10.1016/0021-9797(80)90587-1.

661
662 Grell, G.A., Peckham, S.E., Schmitz, R., McKeen, S.A., Frost, G., Skamarock, W. C., Eder, B., 2005.
663 Fully coupled "online" chemistry within the WRF model. *Atmos. Environ.*, 39, 6957-6975,
664 10.1016/j.atmosenv.2005.04.027.

665
666 Harrison, R.M., Shi, J.P., Xi, S.H., Khan, A., Mark, D., Kinnersley, R., Yin, J. X., 2000.
667 Measurement of number, mass and size distribution of particles in the atmosphere. *Philos. T. R. Soc.*
668 *A*, 358, 2567-2579.

669
670 Harrison, R.M., Beddows, D.C.S., Dall'Osto, M., 2011. PMF analysis of wide-range particle size
671 spectra collected on a major highway. *Environ. Sci.Technol.*, 45, 5522-5528, 10.1021/es2006622.

672
673 Harrison, R.M., Jones, A.M., Beddows, D.C.S., Dall'Osto, M., Nikolova, I., 2016. Evaporation of
674 traffic-generated nanoparticles during advection from source. *Atmos. Environ.*, 125, 1-7,
675 10.1016/j.atmosenv.2015.10.077.

676
677 Harrison, R.M., MacKenzie, A.R., Xu, H.M., Mohammed, S.A., 2018. Diesel exhaust nanoparticles
678 and their behaviour in the atmosphere. *Roy. Soc. Proceed. A*, 474, 1-20, 10.1016/s1001-
679 6058(08)60125-0.

680
681 Harrison, R.M., Beddows, D.C.S., Alam, M.S., Singh, A., Brean, J., Xu, R., Kotthaus, S., Grimmond,
682 S., 2019. Interpretation of particle number size distributions measured across an urban area during
683 the FASTER campaign. *Atmos. Chem.Phys.*, 19, 39-55, 10.5194/acp-19-39-2019.

684
685 Jacobson, M.Z., Seinfeld, J.H., 2004. Evolution of nanoparticle size and mixing state near the point
686 of emission. *Atmos. Environ.*, 38, 1839-1850, 10.1016/j.atmosenv.2004.01.014.

687
688 Jacobson, M. Z., et al.,1996. Simulating equilibrium within aerosols and nonequilibrium between
689 gases and aerosols. *Journal of Geophysical Research-Atmospheres*,101,9079-9091,
690 10.1029/96JD00348.

691
692 Jacobson, M. Z. and R. P. Turco,1995. Simulating Condensational Growth, Evaporation, and
693 Coagulation of Aerosols Using a Combined Moving and Stationary Size Grid. *Aerosol Science and*
694 *Technology*, 22, 73-92, 10.1080/02786829408959729.

695
696 Jacobson, M.Z., 2005. *Fundamentals of Atmospheric Modeling*, Second Edition ed., Cambridge
697 University Press, New York.

698
699 Jacobson, M. Z., Kittelson, D.B., Watts, W.F., 2005. Enhanced coagulation due to evaporation and
700 its effect on nanoparticle evolution. *Environ. Sci.Techn.*, 39, 9486-9492, 10.1021/es0500299.

701
702 Jones, A.M., Harrison, R.M., 2006. Estimation of the emission factors of particle number and mass
703 fractions from traffic at a site where mean vehicle speeds vary over short distances. *Atmos. Environ.*,
704 40, 7125-7137, 10.1016/j.atmosenv.2006.06.030.

705
706 Kuik, F., Lauer, A., Churkina, G., Denier van der Gon, H.A.C., Fenner, D., Mar, K. A., Butler, T. M.,
707 2016. Air quality modelling in the Berlin–Brandenburg region using WRF-Chem v3.7.1: sensitivity
708 to resolution of model grid and input data. *Geosci. Model Dev.*, 9, 4339-4363, 10.5194/gmd-9-4339-
709 2016.

710
711 Kumar, P., Morawska, L., Birmili, W., Paasonen, P., Hu, M., Kulmala, M., Harrison, R.M., Norford,
712 L., Britter, R., 2014. Ultrafine particles in cities. *Environ. Int.*, 66, 1-10,
713 10.1016/j.envint.2014.01.013.

714
715 Kwak, K. H., Baik, J.J., 2014. Diurnal variation of NO_x and ozone exchange between a street canyon
716 and the overlying air. *Atmos. Environ.*, 86, 120-128, 10.1016/j.atmosenv.2013.12.029.

717
718 LeGrand, S. L., Polashenski, C., Letcher, T. W., Creighton, G. A., Peckham, S. E., Cetola, J. D., 2019.
719 The AFWA dust emission scheme for the GOCART aerosol model in WRF-Chem v3.8.1. *Geosci.*
720 *Model Dev.*, 12, 131-166, 10.5194/gmd-12-131-2019.

721
722 Manigrasso, M., Natale, C., Vitali, M., Protano, C., Avino, P., 2017. Pedestrians in traffic
723 environments: Ultrafine particle respiratory doses. *Int. J. Environ. Res. Public Health*, 14,
724 10.3390/ijerph14030288.

725
726 McHugh, C.A., Carruthers, D.J., Edmunds, H.A., 1997. ADMS-Urban: an air quality management
727 system for traffic, domestic and industrial pollution. *Int. J. Environ. Pollut.*, 8, 666-674.

728
729 Moeng, C.H., Dudhia, J., Klemp, J., Sullivan, P., 2007. Examining two-way grid nesting for large
730 eddy simulation of the PBL using the WRF model. *Mon. Weather Rev.*, 135, 2295-2311,
731 10.1175/mwr3406.1.

732
733 Munir, S., Habeebullah, T. M., 2015. Vehicular emissions on main roads in Makkah, Saudi Arabia
734 dispersion modelling study. *Arab. J.Geosci.*, 11, 10.1007/s12517-018-3857-z, 2018.

735
736 Munoz-Esparza, D., Kosovic, B., van Beeck, J., Mirocha, J., 2015. A stochastic perturbation method
737 to generate inflow turbulence in large-eddy simulation models: Application to neutrally stratified
738 atmospheric boundary layers. *Phys. Fluids*, 27, 10.1063/1.4913572.

739
740 Nikolova, I., MacKenzie, A. R., Cai, X. M., Alam, M. S., Harrison, R. M., 2016. Modelling
741 component evaporation and composition change of traffic-induced ultrafine particles during travel
742 from street canyon to urban background. *Faraday Discuss.*, 189, 529-546, 10.1039/c5fd00164a.

743
744 Nikolova, I., Cai, X., Alam, M.S., Zeraati-Rezaei, S., Zhong, J., MacKenzie, A. R., Harrison, R. M.,
745 2018. The influence of particle composition upon the evolution of urban ultrafine diesel particles on
746 the neighbourhood scale. *Atmos. Chem. Phys. Discuss.*, 18, 1-39, 10.5194/acp-2017-1018.

747
748 Nottrott, A., Kleissl, J., and Keeling, R.: Modeling passive scalar dispersion in the atmospheric
749 boundary layer with WRF large-eddy simulation, *Atmospheric Environment*, 82, 172-182,
750 10.1016/j.atmosenv.2013.10.026, 2014.

751
752 Nunalee, C. G., Kosovic, B., and Bieringer, P. E.: Eulerian dispersion modeling with WRF-LES of
753 plume impingement in neutrally and stably stratified turbulent boundary layers, *Atmospheric*
754 *Environment*, 99, 571-581, 10.1016/j.atmosenv.2014.09.070, 2014.

755

756 Panis, L. I., de Geus, B., Vandenbulcke, G., Willems, H., Degraeuwe, B., Bleux, N., Mishra, V.,
757 Thomas, I., and Meeusen, R.: Exposure to particulate matter in traffic: A comparison of cyclists and
758 car passengers, *Atmospheric Environment*, 44, 2263-2270, 10.1016/j.atmosenv.2010.04.028, 2010.
759

760 Pankow, J. F.: An absorption model of gas/particle partitioning of organic compounds in the
761 atmosphere, *Atmospheric Environment*, 28, 185-188, 10.1016/1352-2310(94)90093-0, 1994.
762

763 Popoola, O. A. M., Carruthers, D., Lad, C., Bright, V. B., Mead, M. I., Stettler, M. E. J., Saffell, J.
764 R., and Jons, R. L.: Use of networks of low cost air quality sensors to quantify air quality in urban
765 settings, *Atmospheric Environment*, 194, 58-70, 10.1016/j.atmosenv.2018.09.030, 2018.
766

767 Pugh, T. A. M., Cain, M., Methven, J., Wild, O., Arnold, S. R., Real, E., Law, K. S., Emmerson, K.
768 M., Owen, S. M., Pyle, J. A., Hewitt, C. N., and MacKenzie, A. R.: A Lagrangian model of air-mass
769 photochemistry and mixing using a trajectory ensemble: the Cambridge Tropospheric Trajectory
770 model of Chemistry And Transport (CiTTyCAT) version 4.2, *Geoscientific Model Development*, 5,
771 193-221, 10.5194/gmd-5-193-2012, 2012.

772 Schell, B., Ackermann, I. J., Hass, H., Binkowski, F. S., and Ebel, A.: Modeling the formation of
773 secondary organic aerosol within a comprehensive air quality model system, *Journal of Geophysical
774 Research-Atmospheres*, 106, 28275-28293, 10.1029/2001jd000384, 2001.
775

776 Skamarock, W. C., and Klemp, J. B.: A time-split nonhydrostatic atmospheric model for weather
777 research and forecasting applications, *Journal of Computational Physics*, 227, 3465-3485,
778 10.1016/j.jcp.2007.01.037, 2008.
779

780 Topping, D., Barley, M., Bane, M. K., Higham, N., Aumont, B., Dingle, N., and McFiggans, G.:
781 UManSysProp v1.0: an online and open-source facility for molecular property prediction and
782 atmospheric aerosol calculations, *Geoscientific Model Development*, 9, 899-914, 10.5194/gmd-9-
783 899-2016, 2016.
784

785 US EPA: NAAQS Table, <https://www.epa.gov/criteria-air-pollutants/naaqs-table>, 10.1016/s1352-
786 2310(01)00438-1, 2017.
787

788 Vu, T. V., Zauli-Sajani, S., Poluzzi, V., Delgado-Saborit, J. M., and Harrison, R. M.: Loss processes
789 affecting submicrometer particles in a house heavily affected by road traffic emissions, *Aerosol
790 Science and Technology*, 51, 1201-1211, 10.1080/02786826.2017.1343453, 2017.
791

792 Zaveri, R. A., Easter, R. C., Fast, J. D., and Peters, L. K.: Model for Simulating Aerosol Interactions
793 and Chemistry (MOSAIC), *Journal of Geophysical Research: Atmospheres*, 113,
794 10.1029/2007jd008782, 2008.
795

796 Zhong, J., Nikolova, I., Cai, X., MacKenzie, A. R., and Harrison, R. M.: Modelling traffic-induced
797 multicomponent ultrafine particles in urban street canyon compartments: Factors that inhibit mixing,
798 *Environmental Pollution*, 238, 186-195, <https://doi.org/10.1016/j.envpol.2018.03.002>, 2018.
799

800

801 **TABLE LEGEND:**

802

803 **Table 1.** Initial/background partial pressure (derived from vapour concentrations on a urban
804 background site) and saturation vapour pressures estimated at temperature of 284.15
805 K based on the UManSysProp online tool using data from Compernelle et al. (2011).
806

807

808 **FIGURE LEGENDS:**

809

810 **Figure 1.** Total UFP number concentration ($\# \text{ cm}^{-3}$): Vertical slice of (a) mean concentration
811 (C_m) and (b) the ratio of concentration fluctuation intensity to mean concentration
812 (C'/C_m); (c) mean concentration with fluctuations along South-North line (starting
813 from 200 m before the emission) at the bottom level.
814

815 **Figure 2.** (a) UFP number-size distribution $dN/d\log D_p$ ($\# \text{ cm}^{-3}$) (fluctuation intensity indicated
816 by shaded areas) for rooftop and its downwind neighbourhood at the bottom level; The
817 inflowing background is taken from 200 m before the emission at the bottom level of
818 the domain; The size-dependent emission flux $dE/d\log D_p$ is shown for comparison. (b)
819 Dilution ratio for the downwind locations; Dashed lines represent the dilution ratio for
820 a passive-like scalar (e.g. total UFP number concentration) at each downwind
821 locations. Rooftop +100 m and +400 m represent the travelling time of about 50 m and
822 200 s, respectively, in this study.
823

824 **Figure 3.** SVOCs concentration (ng m^{-3}) (fluctuation information indicated by shaded areas) at
825 the rooftop and its downwind neighbourhood locations at the bottom level: (a) Gas
826 concentrations; (b) Particle concentrations, (c) Sum of gas and particle concentrations
827 and (d) Dilution ratio for the downwind locations (The absolute concentrations for
828 high-carbon gas-phase components and for low-carbon particle-phase components are
829 very close to the background concentrations; therefore the dilution ratios for these
830 components are not shown.); Dash lines represent the dilution ratio for a passive-like
831 scalar (also indicated in Figure 4b) at each downwind locations. Rooftop +100 m and
832 +400 m represent the travelling time of about 50 m and 200 s, respectively, in this
833 study.
834

835 **Figure 4.** Scaled total UFP number concentration along South-North line at the bottom level.
836

837 **Figure 5.** (a) Scaled UFP number-size distributions and (b) ϕ for selected bins (bins 3, 5 and 7
838 with bin bounds of [10.7 nm, 14.6 nm], [19.8 nm, 26.9 nm] and [36.6 nm, 49.9 nm],
839 respectively) at rooftop+400m (or travelling time of about 200 s) for the bottom level.
840

841 **Figure 6.** Scaled SVOC (a) gas concentrations, (b) particle concentrations, (c) the sum of both
842 gas and particle concentrations and (d) Correction factor for a typical SVOC C25 for
843 rooftop+400m (or travelling time of about 200 s) at the bottom level.
844

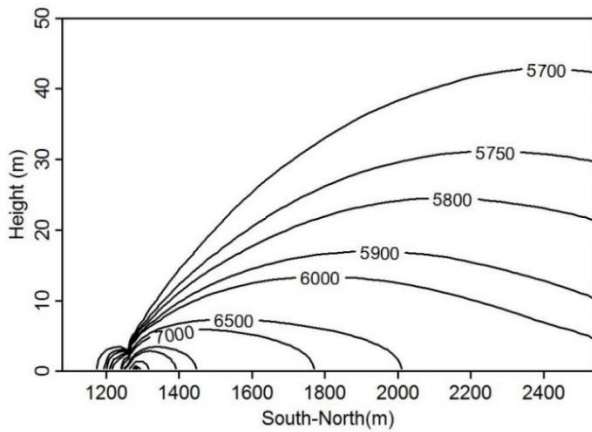
845 **Table 1.** Initial/background partial pressure (derived from vapour concentrations on an urban
846 background site) and saturation vapour pressures estimated at temperature of 284.15 K based on the
847 UManSysProp online tool using data from Compernelle et al. (2011).

N-alkanes	Partial pressure (in Pa)	Saturation vapour pressure at 284.15 K (in Pa)
C16	1.19E-007	6.42E-02
C17	8.90E-008	1.91E-02
C18	4.44E-008	5.69E-03
C19	2.77E-008	1.70E-03
C20	1.20E-008	5.05E-04
C21	4.16E-009	1.50E-04
C22	1.29E-008	4.48E-05
C23	1.73E-008	1.33E-05
C24	2.29E-008	3.97E-06
C25	1.76E-008	1.18E-06
C26	8.74E-009	3.52E-07
C27	5.73E-009	1.05E-07
C28	5.80E-009	3.12E-08
C29	3.57E-009	9.30E-09
C30	2.73E-009	2.77E-09
C31	4.46E-009	8.25E-10
C32	4.31E-009	2.46E-10

848

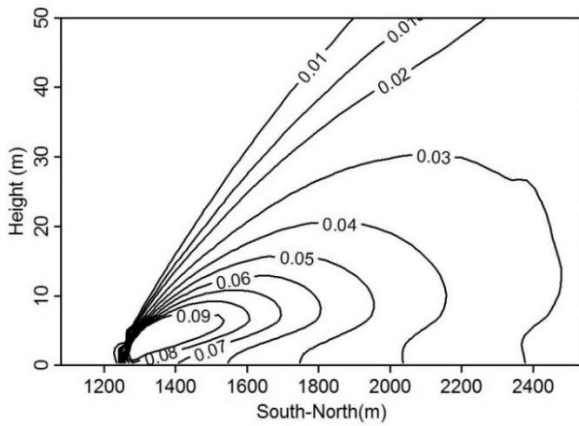
849

850 (a) C_m (# cm^{-3})



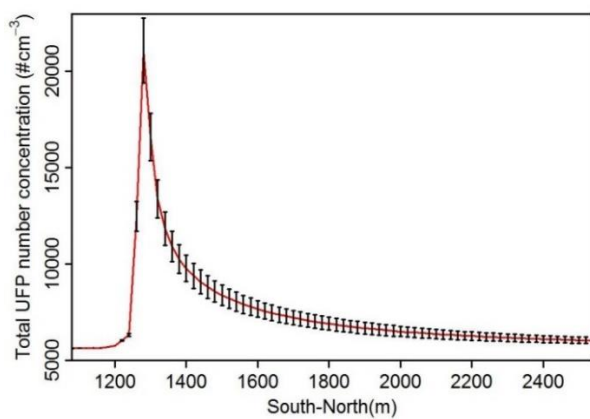
851

852 (b) C'/C_m



853

854 (c) $C_m \pm C'$ along the South-North line

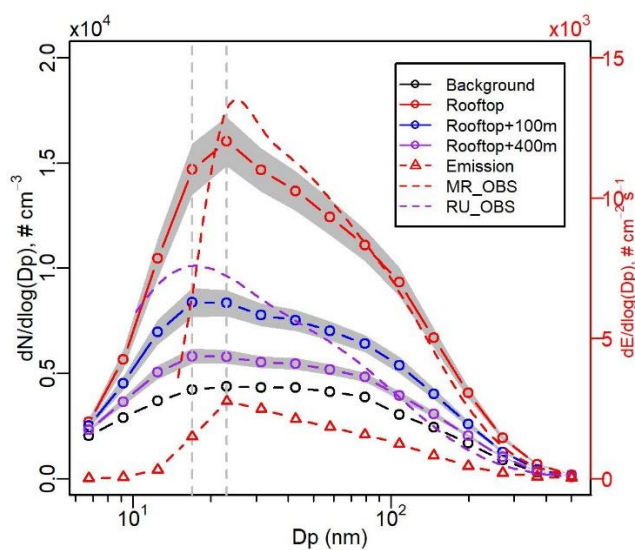


855

856 **Figure 1.** Total UFP number concentration (cm^{-3}): Vertical slice of (a) mean concentration (C_m)
857 and (b) the ratio of concentration fluctuation intensity to mean concentration (C'/C_m); (c) mean
858 concentration with fluctuations along South-North line (starting from 200 m before the emission) at
859 the bottom level from the model.

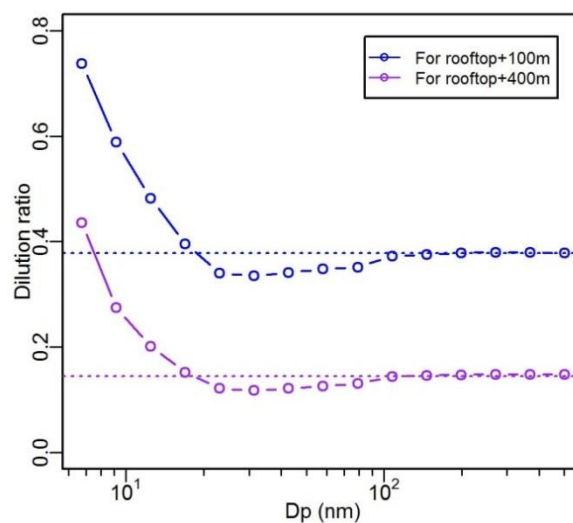
860

(a)



861

(b)

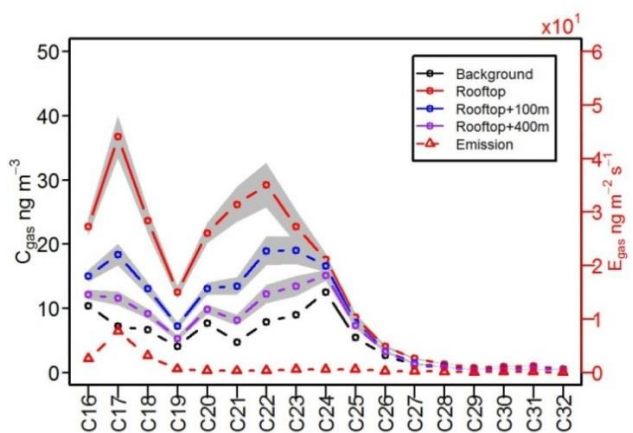


862 **Figure 2.** (a) UFP number-size distribution $dN/d\log D_p$ ($\# \text{ cm}^{-3}$) (fluctuation intensity indicated by
 863 shaded areas) for rooftop and its downwind neighbourhood at the bottom level; The inflowing
 864 background is taken from 200 m before the emission at the bottom level of the domain; The size-
 865 dependent emission flux $dE/d\log D_p$ is shown for comparison; MR_OBS represents the measurement
 866 from Marylebone roadside; RU_OBS represents the measurement from the nearby downwind rooftop
 867 location. (b) Dilution ratio for the downwind locations; Dashed lines represent the dilution ratio for a
 868 passive-like scalar (e.g. total UFP number concentration) at each downwind locations. Rooftop +100
 869 m and +400 m represent the travelling time of about 50 m and 200 s, respectively, in this modelling
 870 study.

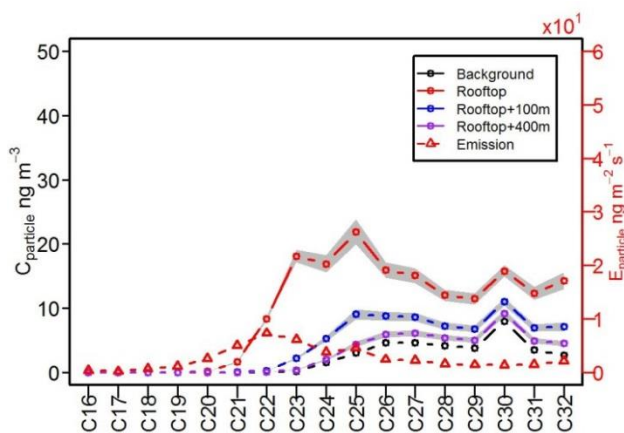
871

872

(a)



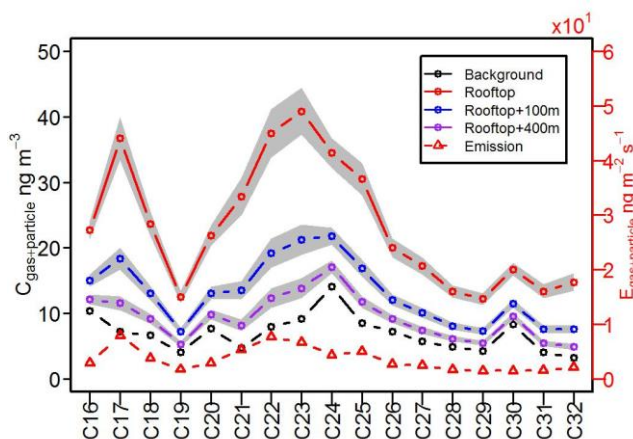
(b)



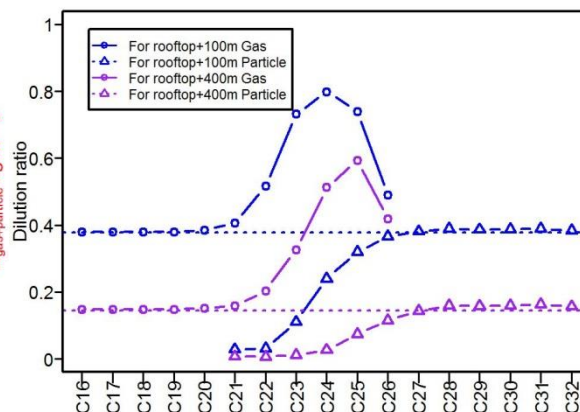
873

874

(c)



(d)



875

876

877

878

879

880

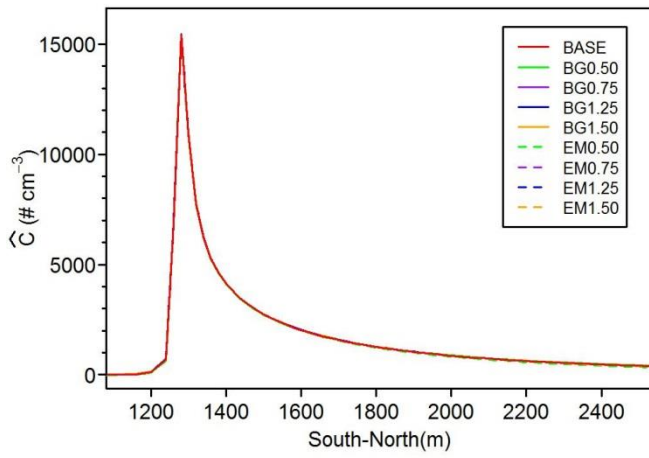
881

882

883

884

Figure 3. SVOCs concentration (ng m^{-3}) (fluctuation information indicated by shaded areas) at the rooftop and its downwind neighbourhood locations at the bottom level: (a) Gas concentrations; (b) Particle concentrations, (c) Sum of gas and particle concentrations and (d) Dilution ratio for the downwind locations (The absolute concentrations for high-carbon gas-phase components and for low-carbon particle-phase components are very close to the background concentrations; therefore the dilution ratios for these components are not shown.); Dash lines represent the dilution ratio for a passive-like scalar (also indicated in Figure 4b) at each downwind locations. Rooftop +100 m and +400 m represent the travelling time of about 50 m and 200 s, respectively, in this modelling study.



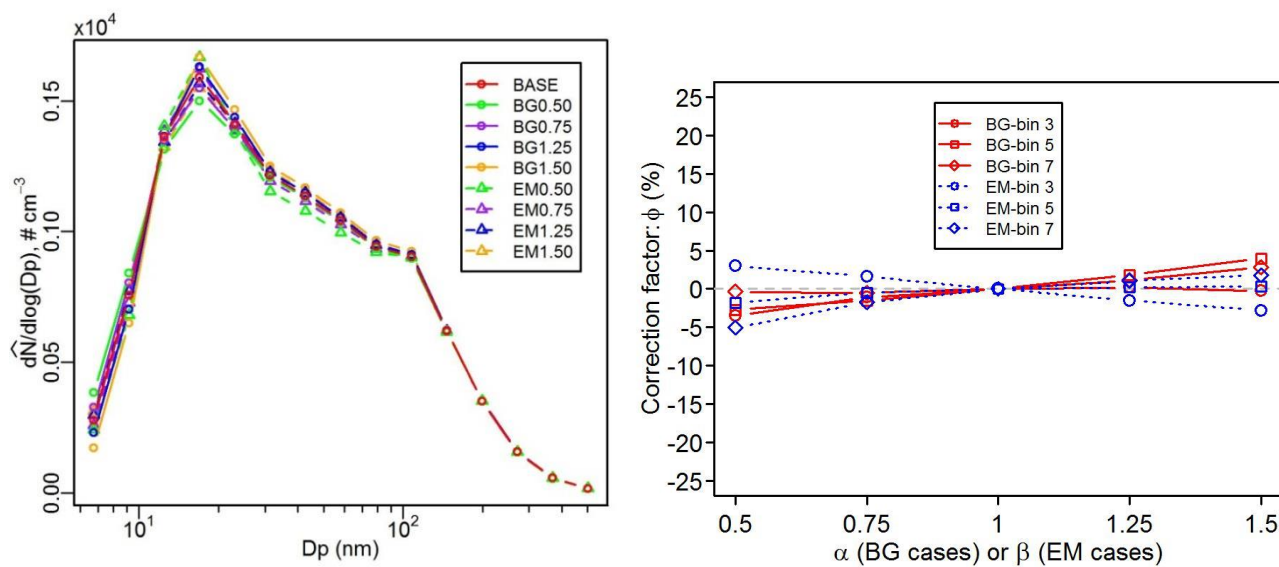
885

886 **Figure 4.** Scaled total UFP number concentration along South-North line at the bottom level from
887 the model.

888

889

890

(a) $d\hat{N}/d\log(D_p)$ at rooftop+400m(b) ϕ for selected bins at rooftop+400m

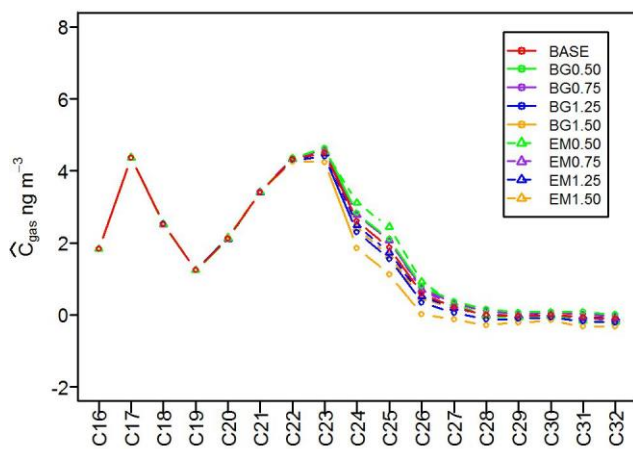
891

892 **Figure 5.** (a) Scaled UFP number-size distributions and (b) ϕ for selected bins (bins 3, 5 and 7 with
 893 bin bounds of [10.7 nm, 14.6 nm], [19.8 nm, 26.9 nm] and [36.6 nm, 49.9 nm], respectively) at
 894 rooftop+400m (or travelling time of about 200 s) for the bottom level from the model.

895

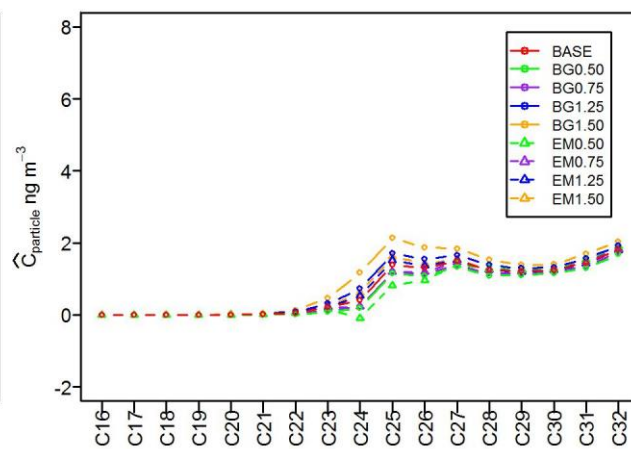
896

897 (a) \hat{C}_{gas} at rooftop+400m



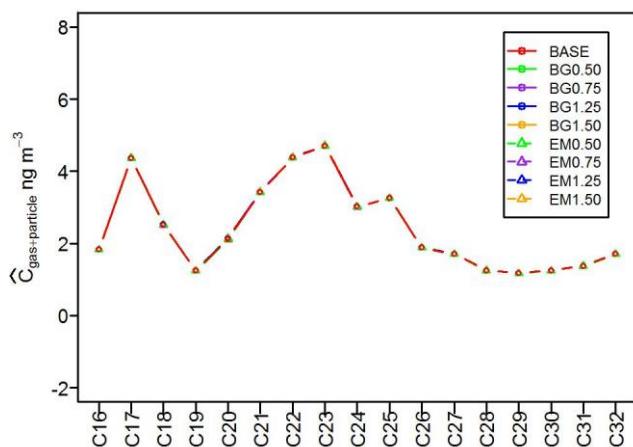
898

(b) $\hat{C}_{particle}$ at rooftop+400m



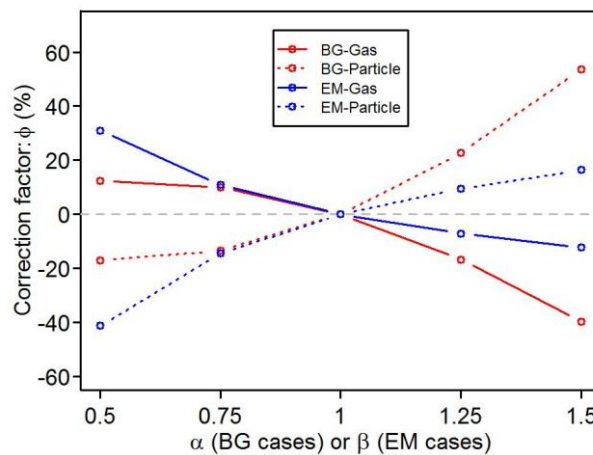
899

900 (c) $\hat{C}_{gas+particle}$ at rooftop+400m



901

(d) ϕ for C25 at rooftop+400m



902 **Figure 6.** Scaled SVOC (a) gas concentrations, (b) particle concentrations, (c) the sum of both gas
903 and particle concentrations and (d) Correction factor for a typical SVOC C25 for rooftop+400m (or
904 travelling time of about 200 s) at the bottom level from the model.

905

906

907